International Journal of Multiphase Flow 36 (2010) 385–396

Contents lists available at ScienceDirect

International Journal of Multiphase Flow

journal homepage: www.elsevier.com/locate/ijmulflow

Studying disturbance waves in vertical annular flow with high-speed video

D. Schubring [a,b,*], T.A. Shedd [b], E.T. Hurlburt [c]

[a] Visualization, Imaging, and Computation of Thermohydraulics for Reactors (VICTR) Lab, University of Florida, 202 Nuclear Science Building, P.O. Box 118300, Gainesville, FL 32611-8300, USA
[b] Multiphase Flow Visualization and Analysis Laboratory (MFVAL), University of Wisconsin-Madison, 1500 Engineering Drive, Madison, WI 53706-1609, USA
[c] Bettis Laboratory West Mifflin, PA 15122, USA

ARTICLE INFO

Article history:
Received 24 August 2009
Received in revised form 6 January 2010
Accepted 6 January 2010
Available online 13 January 2010

Keywords:
Disturbance waves
Vertical flow
Annular flow
Visualization

ABSTRACT

In many annular two-phase gas–liquid flows, large disturbance waves propagate liquid mass. These waves are important for modeling of gas-to-liquid momentum transfer and liquid film behavior. High-speed videos of vertical upflow have been analyzed to extract individual and average wave data. Two types of structures, coherent waves and piece waves, have been identified in these flows. Velocities, lengths, and temporal spacings of individual waves and average velocities, lengths, frequencies, and intermittencies have been studied as functions of both gas and liquid flow rates. Velocity and frequency increase with liquid and gas flow rates, length decreases with increasing gas flow and increases with increasing liquid flow, and intermittency is predominantly an increasing function of liquid flow.

1. Introduction

Disturbance waves are among the most dramatic phenomena in two-phase gas–liquid annular flow. Waves have been treated as a component of the film, as a type of entrainment, and as a separate type of liquid flow in the literature, depending on which phenomenon is being studied. The third approach is used in the wave data analysis in this work.

Azzopardi has studied disturbance waves in annular flow in some detail, including a review article on wave statistics in 1986 (Azzopardi, 1986) and an update to this work as part of a larger review of droplet behavior in 1997 (Azzopardi, 1997). Wave velocities and frequencies in vertical upflow increase with increasing gas and liquid flow rates, according to Nedderman and Shearer (1963) and Hall Taylor et al. (1963). Martin (1983) studied diameter effects, observing an inverse relationship between diameter and wave frequency and no strong relationship between wave velocity and diameter. Mori et al. (1999) described an inverse relationship between liquid kinematic viscosity and wave frequency in vertical flow. Recently, Sawant et al. (2008) investigated disturbance waves at vertical air–water flow, using two conductance probe traces. Revised, non-dimensional correlations for wave frequency and velocity were developed for these data, including flow conditions at elevated pressures (1.2, 4.0, and 5.8 bar).

Pearce (1979) developed a mechanistic model and an empirical correlation for wave velocity, v_{wave}. Pearce's empirical correlation is provided as:

$$v_{wave,Pearce} = \frac{U_{l,i} + U_g\sqrt{\frac{\rho_g}{\rho_l}}}{1+\sqrt{\frac{\rho_g}{\rho_l}}} \tag{1}$$

The gas and liquid densities are included in this equation (ρ_g and ρ_l, respectively). The velocity at the liquid surface, $U_{l,i}$, is a challenging measurement (indeed, more challenging than direct measurement of wave velocity) and is not available for the present data. In addition, the gas velocity, U_g, must be estimated if void fraction data are not available.

Swanson (1966) asserted that gas friction velocity ($v_{fric,g}$, Eq. (2)) was equal to wave velocity, v_{wave}, for his data, while Sawai et al. (1989) attempted correlation to the liquid friction velocity (u^*, Eq. (3)). In these equations, τ_w is the wall shear.

$$v_{fric,g} = \sqrt{\frac{\tau_w}{\rho_g}} \tag{2}$$

$$u^{\star} = \sqrt{\frac{\tau_w}{\rho_l}} \tag{3}$$

Wave frequency modeling, such as that by Hall Taylor and Nedderman (1968) and Azzopardi (1986), has focused on using the wave velocity distribution to predict wave coalescence. Waves with a wider velocity distribution are more likely to collide and coales-

* Corresponding author. Address: 202 Nuclear Science Building, P.O. Box 118300, Gainesville, FL 32611-8300, USA. Tel.: +1 352 392 1401x314; fax: +1 352 392 3380.
E-mail address: dlschubring@ufl.edu (D. Schubring).

0301-9322/$ - see front matter © 2010 Elsevier Ltd. All rights reserved.
doi:10.1016/j.ijmultiphaseflow.2010.01.003

cence, while those with a very narrow distribution will maintain their space along the pipe. Shearer (1964) recommends two dimensionless numbers for correlation of wave frequency, f_{wave}: a Strouhal number (Sr_{wave}) and a liquid film Reynolds number ($Re_{l,film}$).

$$Sr_{wave} = \frac{f_{wave} D}{U_{sg}} \tag{4}$$

$$Re_{l,film} = \frac{\dot{m}_l}{D\pi\mu_l} \tag{5}$$

Sr_{wave} is defined using the gas superficial velocity (volumetric flux), U_{sg}, and tube diameter, D. $Re_{l,film}$ also employs the liquid mass flow rate, $\dot{m}_l$, and dynamic viscosity, μ_l.

Some work has suggested multiple types of disturbance waves exist in annular flow. Mori et al. (1996, 1999) observed a second type of wave structure, termed "huge waves", near the annular-churn transition boundary. These waves are said to carry more mass and travel at a larger velocity than disturbance waves. Hawkes et al. (2000) explored what they termed wispy-annular flow at higher liquid flows than in the present study. Again, two types of wave structures were identified, with "wisps" traveling at a higher velocity than disturbance waves, but at a lower frequency. Some of the present authors recently explored and correlated horizontal wave data (f_{wave} and v_{wave}) using a similar LED/phototransistor apparatus as Hawkes et al. (Schubring and Shedd, 2008).

The present study is a quantitative visualization of disturbance waves in vertical annular flow through the use of high-speed videos. There are two primary objectives to the study:

1. Demonstrate the use of high-speed video to estimate the velocities, lengths, and temporal spacings of *individual waves* – measurements not available from the traditional conductance probe or LED-based estimates of wave statistics.
2. Use these individual wave measurements to better understand the distribution of disturbance waves and, in turn, annular flow as a whole.

2. Experimental

A schematic of the flow loop is shown in Fig. 1. Compressed air was run through an oil/particulate filter prior to flowing through two identical air rotameters. Each had a maximum nominal volumetric flow rate ($Q_{g,nom}$) of 1400 L min^{-1} and an uncertainty of 70 L min^{-1}. One air controller was used for all flows at or below 1200 nominal L min^{-1} and was set to read 1200 L min^{-1} for flow rates above this, with the second air controller adjusted to produce the desired nominal air flow rate. Uncertainties at and above 1400 nominal L min^{-1} are estimated at 100 L min^{-1}. $Q_{g,nom}$ is adjusted to actual gas mass flow rate, $\dot{m}_g$, using:

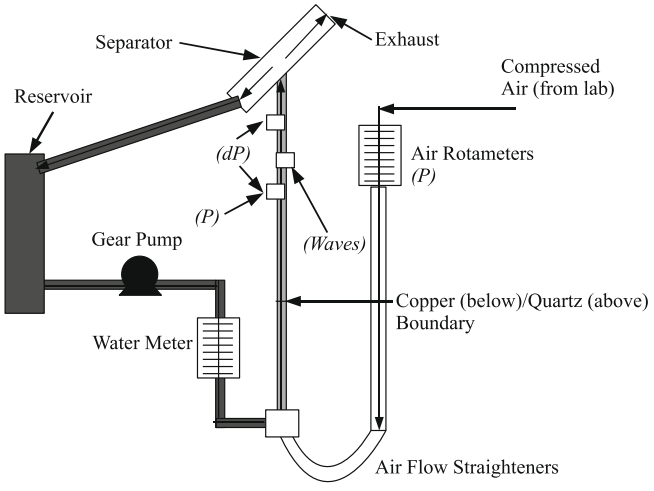

Fig. 1. Diagram of flow loop.

$$Q_{g,meter} = Q_{g,nom}\sqrt{\frac{P_{std}}{P_{meter}}} \tag{6}$$

$$\dot{m}_g = \rho_{g,meter} Q_{g,meter} \tag{7}$$

A Cole–Parmer stainless steel pressure diaphragm transducer was used at the air meters to measure the local gauge pressure and to compute the P_{meter} (absolute meter pressure). Pressure data were fed to a PC through a Agilent 34790A data acquisition system. The manufacturer-specified uncertainty is 830 Pa. A standard pressure, P_{std}, of 101.35 Pa (14.7 lbf in^{-2}) was employed in Eq. (6), as recommended by the manufacturer.

City water entered a PVC reservoir through particulate and deionizing filters. Up to 10 L min^{-1} of water was provided to the loop with a gear pump. Water flowed through a 200 μm filter before the pump and an 80 μm filter after it prior to a Coriolis meter with digital display and uncertainty of 0.1 L min^{-1}, dominated by visual uncertainty on the meter.

Prior to mixing, the air passed through flow straighteners beneath the loop as it turned upward. Water was introduced perpendicular to the air flow through several 2 mm holes. The two-phase mixture flowed in a 23.7 mm ID copper development length approximately 2 m long. The flow encountered a weak contraction to the quartz test section (23.4 mm) and was allowed to develop a further 1.7 m before the center of the test section. A development length based on this location is approximately 150 L/D.

Based on the work of Wolf et al. (2001), 100 L/D is sufficient for wave behavior development. However, Wolf et al. considered only gross statistics estimates from signal cross-correlation. It is possible that the more detailed, individual wave statistics require greater development length. Further, the re-development necessary after the contraction may adversely affect the degree to which the flow in the test section was developed. As a result, the behavior documented in this work may not be fully developed and further work is advised to verify the L/D required.

To estimate test section conditions accurately, differential pressure and absolute pressure measurements were taken. The upstream pressure tap was also used for an absolute pressure measurement, taken using the same type of equipment as the measurement at the air meter. Flow rates and fluid properties were evaluated based on this absolute pressure less half the differential pressure found.

Considering all sources of uncertainty regarding flow rates and pressures, typical total uncertainties for U_{sg} and U_{sl} are estimated as 10–15% and 5%, respectively; a 5–10% uncertainty on pressure gradient is estimated. A type T thermocouple was placed in a separator above the test section to better estimate fluid properties.

The high-speed wave videos were taken using an Integrated Design Tools X-Stream VISION XS-3 high-speed CMOS digital camera that imaged in 8-bit grayscale. The camera was placed on the opposite side of the tube from five bright lights, visible on the videos. As waves or entrained droplets pass through the visualization section, they can seen in the images as dark spots. Images showing a ruler were also taken to allow for the conversion to a physical scale. The pixels were 242 μm squares (30.3 cm total axial length). The total image resolution was 1252 pixels (axial length) by 112 or 120 pixels (width), cropped from the camera's maximum 1300 by 1030.

A grid of 5 air and 11 water meter readings ($Q_{g,nom}$ and Q_l) were considered. Gas meter readings of 800, 1000, 1200, 1400, and 1600 nominal L min^{-1} and water meter readings of 1, 1.5, 2, 3, 4, 5, 6, 7, 8, 9, and 10 L min^{-1} were used. The frame rate was set to one-half of the air meter reading $Q_{g,nom}$, based on previous investigations that indicated wave velocity increases with increasing gas flow. To maintain similar frame counts for all flow conditions, videos with air flows ($Q_{g,nom}$) of 800 L min^{-1}, 1000 L min^{-1}, 1200 L min^{-1}, 1400 L min^{-1}, and 1600 L min^{-1} were 11 s, 10 s, 9 s, 8 s, and 7 s long, respectively. Those flows with water meter readings of 10 L min^{-1} used videos 120 pixels wide; all other videos are 112 pixels wide. One video ($Q_l = 8$ L min^{-1}, $Q_{g,nom} = 800$ L min^{-1}) was unusable due to an object passing between the camera and test section, leaving 54 flow conditions.

3. Vertical wave processing

The image sequences were processed using MATLAB to provide estimates of gross wave statistics (average velocity, frequency, etc.) and to identify and characterize individual waves. The steps in this processing are outlined below.

3.1. Virtual detectors

Several "detectors" were placed at selected locations in each of the images to virtualize the LED/phototransistor array from Schubring and Shedd (2008). The darkening of the image as a wave passed over these detectors produced a change in average pixel value.

Locations corresponding to the five lights in the images were selected, identified at pixel locations (from the left edge) of 145, 365, 570, 835, and 1120 (3.51, 8.83, 13.79, 20.21, and 27.10 cm). These detectors were labeled 1–5 in increasing pixel location (i.e., opposite the direction of flow). Since no radial variations were considered in this work, the detector signal was taken as an average brightness within its boundaries (11 pixels in axial length and the full width of the image).

Each signal was inverted so that the largest possible value (255) corresponded to a saturated black image and the smallest possible value (0) corresponded to a saturated white image. This detector signal was termed $Dark(det, t)$, a function of detector number (det) and time/frame number (t). Since it is desirable for waves to have similar signals in each detector, a normalized darkness ($Dark_{norm}(Det, t)$) was defined as:

$$Dark_{norm}(Det, t) = \frac{Dark(Det, t) - \overline{Dark(Det)}}{s(Dark(Det))} \quad (8)$$

The time-average for each detector is represented by $\overline{Dark(Det)}$, with $s(Dark(Det))$ denoting the standard deviation.

3.2. Example signals and images

Fig. 2 shows the normalized signals from all detectors for a segment of the flow with U_{sg} of 42.3 m s^{-1} and U_{sl} of 15.5 cm s^{-1}. At left, one second of data is shown. Waves are identified by sharp spikes upward in $Dark_{norm}$. Values of $Dark_{norm}$ below −2 are generally not seen; conversely, spikes to and above 4 are fairly common. Close examination of this figure indicates that very large spikes in one detector are often accompanied by similar spikes in other detectors (such as the groupings at around 5.18 and 5.50 s). Examination of actual images shows this to be characteristic of a very dark wave that passes over each sensor in sequence. A smaller timespan is shown at right in Fig. 2.

Images corresponding to the one-tenth second signal shown in Fig. 2 are shown in Fig. 3, with each image separated by three frames (6 ms) from the one above. Three waves were detected passing over detector 3 (center light) in this 100 ms span; they are readily apparent in the images in Fig. 3 as dark structures that move from right-to-left in successive images at an approximately constant velocity.

It is instructive to examine the graph in Fig. 2 along with these images. The first wave passing over the center light (detector 3) is noted in the graph at the beginning of the timespan. It is also noticed in detectors 2 and 1 (in sequence) prior to leaving the test section near 5.24 s. By the time this wave has departed, another has entered the frame and is first observed by detector 5 (farthest right) at 5.23 s.

Other structures are visible in these images, including a small wave, traveling in front of the first large wave. This wave was identified by the code and passed over detector 3 before the timespan shown. It can be seen as a small spike in the graph at 5.208 s in detector 1. Another small wave enters near the beginning of the example images, passing through detectors 5 and 4. It proceeds at a lower velocity than larger waves and is overtaken by the second large wave prior to arrival at detector 3. Another small wave is entering the visualization section at 5.3 s.

3.3. Wave score

While the maximum normalized darkness for a particular wave is similar among detectors, some variability was noted, particularly for waves with smaller peaks. By summing the peak normalized darkness and the two adjacent frames, a more consistent metric was found. This was termed the wave score, defined by:

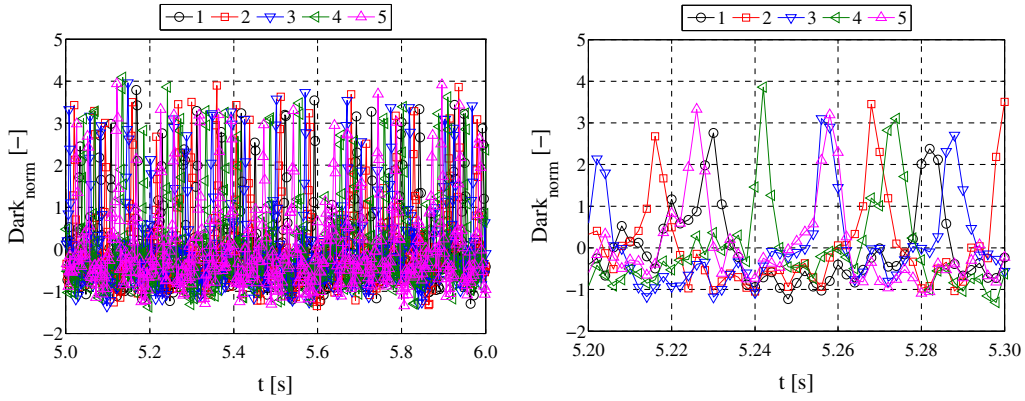

Fig. 2. Example signal traces (U_{sg} of 42 m s^{-1} and U_{sl} of 15.5 cm s^{-1}). (Left) One second of data. (Right) One-tenth second of data.

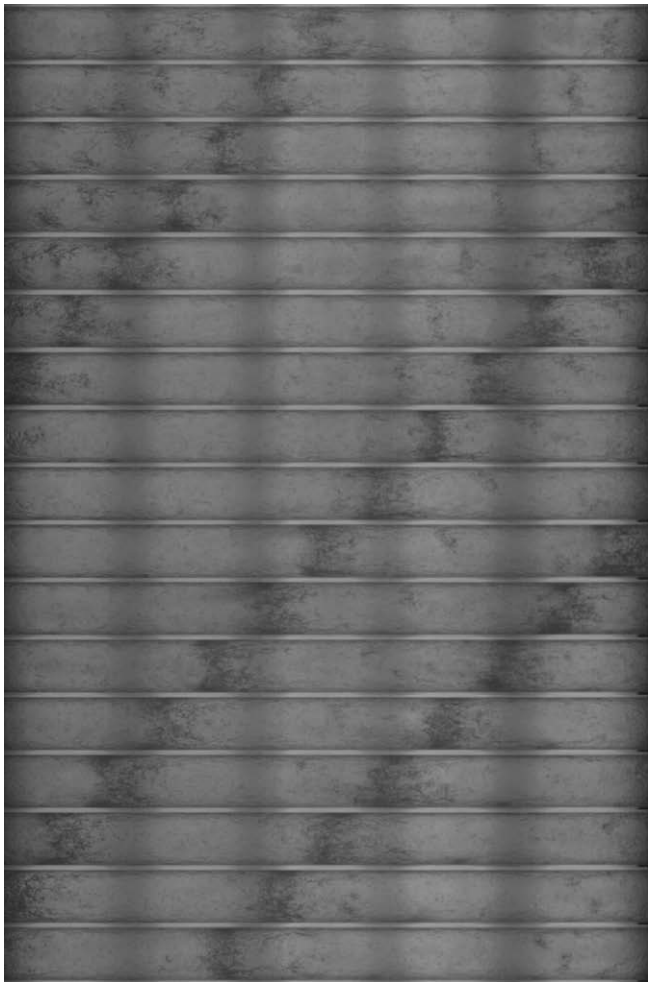

Fig. 3. Example images (U_{sg} of 42 m s^{-1} and U_{sl} of 15.5 cm s^{-1}). Each image is separated from the one above by 6 ms (three frames). Test section shown: 30.3 cm.

$$Score(Det,t) = \sum_{t'=t-1}^{t+1} Dark_{norm}(Det,t') \tag{9}$$

Examples of a wide range of wave scores are shown in Fig. 4. Large wave scores correspond to structures similar to the three large waves in Fig. 3. Wave scores near or below zero do not correspond to waves. Given this observation, a minimum wave score is a reasonable criterion for differentiating between waves and noise. This first critical wave score was set to 0.2 and applied separately to each sensor. The second critical wave score is involved in wave verification after tracking through all detectors (Section 3.6).

Possible waves include a wave score that exceeds this critical value and either:

1. The normalized darkness of a frame is higher than that of the two neighboring frames, each of which is also darker than its other neighbors.
2. The normalized darkness rises for two frames, drops for one frame, increases for one frame, and then drops for two frames.

To match wave score to flow phenomena, the relevance of these phenomena to loss of backlighting visability must be considered. Longer waves will have higher wave scores as they occlude the camera from the backlighting for a longer period. Thicker waves with more entrained bubbles and a rougher surface can also be expected to create a higher wave score. However, the relative importance of these four phenomena (wave length, wave height, bubble entrainment, and surface roughness) on wave score is unclear, particularly among the last three that cannot be decoupled using these videos.

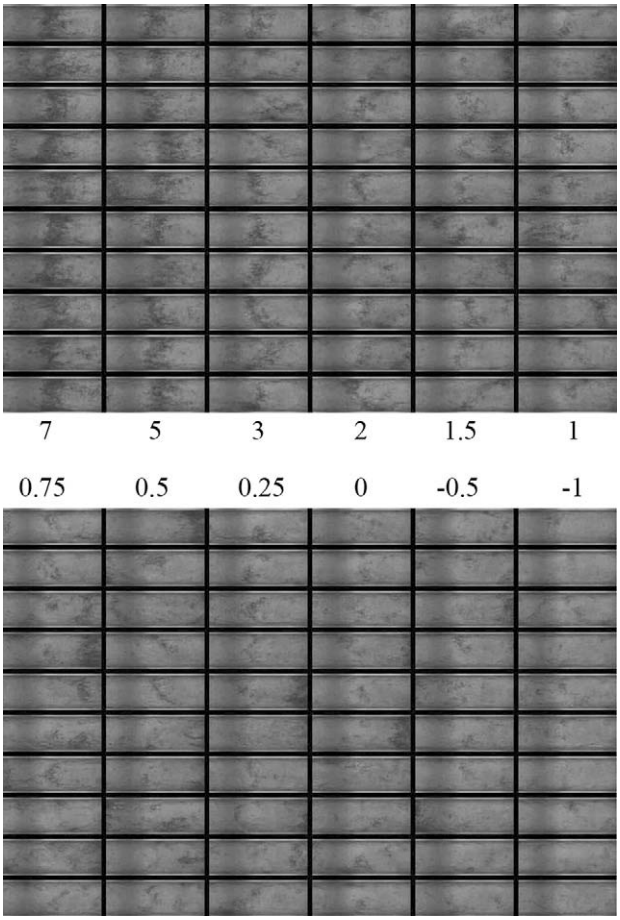

Fig. 4. Typical images in detector 3 (U_{sg} of 42 m s^{-1} and U_{sl} of 15.5 cm s^{-1}), wave scores as labeled.

3.4. Adjustment of wave passing time

The sampling frequency (frame rate) of the videos, while large, is finite. The previous estimate of wave passage time therefore has a quantization error on the order of one frame (2 ms for the example used above). This uncertainty, acceptable for temporal spacings, propagates to wave velocity. As an example, the average wave in this flow takes 30 frames (60 ms) to pass between detectors 1 and 5. A one-frame quantization error produces an uncertainty of 2 ms, leading to a 3% uncertainty in wave velocity.

While the waves seen in the present work are not generally perfectly symmetric, a passage time adjustment to five-frame wave structures was found to produce better linear correlation of passage time and detector locations. This procedure nudges the estimated passage time by up to one-half frame, as shown in Eq. (10) (used when the following frame is darker) and (11) (used when the leading frame is darker). The updated time (frame) of passage is termed t_{wave}, with the initial estimate (quantized to one frame) termed t. No adjustment is made to seven-frame wave structures.

$$t_{wave} = t + 0.5\frac{Dark_{norm}(Det,t+1/fps) - Dark_{norm}(Det,t-1/fps)}{Dark_{norm}(Det,t) - Dark_{norm}(Det,t-1/fps)} \tag{10}$$

$$t_{wave} = t - 0.5\frac{Dark_{norm}(Det,t-1/fps) - Dark_{norm}(Det,t+1/fps)}{Dark_{norm}(Det,t) - Dark_{norm}(Det,t+1/fps)} \tag{11}$$

This adjustment yields produces an essentially continuous estimate of velocity by a linear regression of passage times (discussed below). The correlation coefficients of these linear regressions are significantly improved from those using only the frame-wise estimates of passage time, suggesting an improvement in wave passage time identification. An assumption implicit in this adjustment is that waves retain their shape (with respect to deflection of backlighting) through the visualization section.

3.5. Wave tracking

Wave tracking begins with detector 5, at the right (upstream) edge of images. Each wave candidate noted here is analyzed in turn. Candidate matching waves in detector 4 are found assuming that all waves travel between 1 and 10 m s^{-1}. Each matching candidate in detector 4 with passage time consistent with these limits is compared with the detector 5 wave candidate based on agreement with expected arrival time and similarity of wave scores between the two detectors. The expected arrival time requires a first estimate of velocity A cross-correlation on one-half second increments was performed between each pair of detectors as this estimate.

An analogous procedure is used to track waves to detectors 3, 2, and 1. Waves detected at a minimum of three locations are subjected to further verification. If no acceptable candidate is found at any detector, that detector is skipped in the calculation and the passage time at the next detector is estimated based on the most recent velocity estimate.

3.6. Wave verification

Waves are verified by three criteria:

1. The average of the wave scores at each detector, assigning skipped detectors a wave score of zero, must exceed a second critical wave score of 0.5.
2. The estimated wave velocity must be between 1 and 10 m s^{-1} (realistic wave velocities).
3. The correlation coefficient from this regression must meet or exceed a specified value (0.998) to ensure that a single, coherent wave is being tracked.

3.7. Wave length

The length of each verified wave is estimated as it passes over detector 3. The darkest part of the wave is first identified in a range 40 pixels (nearly 1 cm) to either side of the center of this detector. The length of the wave is then found by scanning both in front of and behind the wave. In each direction, axial positions are compared to the local time-averaged darkness. Positions for which the increase in darkness is less than 20% of the maximum (determined above for each wave) or less than 2 levels (of 256 maximum) from the average in the image sequence are identified. When 3 consecutive axial pixel locations, or 10 in total, are found in either direction, the final location is identified as the left or right edge of the wave. The length of the wave is estimated as the difference between the left and right edges.

Two types of spurious results can be obtained with this procedure:

1. Very small waves, particularly those at high gas flows, may not be identified and will return a zero wave length.
2. When the distance between the waves is small, the calculation of wave length may incorrectly identify both waves (and the distance between them) as part of the same wave. This can be especially damaging to the results if both waves of the pair lead to inaccurately large estimate of L_{wave}.

3.8. Calculation of statistics

The average wave velocity is estimated as the ensemble average of the individual waves' estimated velocities. Wave frequency is estimated by counting the number of verified waves and dividing by the number of seconds for which waves were tracked. For both v_{wave} and f_{wave}, the actual uncertainty is dominated by a bias error relating to critical wave scores (below).

Two estimates of average wave length are generated. The first is the ensemble average of individual wave lengths. This estimate may be contaminated by the two types of spurious results discussed in the section above. A second estimate is the median wave length, selected as representative of the actual average wave length as it yields smoother trends with flow rate. The median wave length averages 4% less than the mean value. The uncertainty on average wave length, due to statistical uncertainty and the selection of the median as opposed to the mean, is estimated at 5–10%.

Wave intermittency is estimated by:

$$INT_w = \frac{f_{wave} L_{wave}}{v_{wave}} \tag{12}$$

The relative statistical uncertainty on INT_w, found by error propagation, is approximately 10%.

Another source of error is the selection of the two critical waves scores: $Score_{crit,1}$, used to determine wave candidates from detectors signals; and $Score_{crit,2}$, used to verify tracked waves. Fig. 5 shows the results for v_{wave}, f_{wave}, L_{wave}, and INT_w as both critical wave scores vary.

The uncertainty on f_{wave} due to selection of critical wave score is estimated at 10% for this flow condition. The bias uncertainty on INT_w is dominated by f_{wave} and is of similar magnitude throughout the flows examined (10%), while the bias uncertainty on v_{wave} and L_{wave} is small (less than 5%).

4. Vertical wave results

In this section, a typical flow will be examined in detail, followed by discussion of the trends with changes in flow rates.

4.1. Wave behavior in example flow

The flow with U_{sg} of 42 m s^{-1} and U_{sl} of 15.5 cm s^{-1} is selected for detailed investigation. The average v_{wave} is estimated as 4.17 m s^{-1}, with f_{wave} of 26.9 s^{-1}. A median L_{wave} of 2.79 cm is found, compared to a mean L_{wave} of 2.87 cm. Based on the median wave length, INT_w is estimated at 0.180.

The distributions of individual wave statistics are shown in Fig. 6. Wave velocities are distributed between 3 and 5 m s^{-1}. The distribution is asymmetric, with a peak at approximately 4.4 m s^{-1}. The cross-correlation estimate of velocity found this peak (specifically, 4.37 m s^{-1}).

dt_{wave}, the single-wave analogy to wave frequency, is the difference in passage time, evaluated at detector 5, between that wave and the one following. The mean value of dt_{wave} is the inverse of f_{wave}; for this flow condition, the mean dt_{wave} is 0.0371 s. The distribution of dt_{wave} is wide, ranging from less than 0.01 s to 0.09 s, but is approximately symmetric about the mean.

Typical L_{wave} results are from 2 to 4 cm with a very sharp peak. The distribution of *Score* is not symmetric, with the median *Score* larger than the mean, similar to that for v_{wave}.

The correlations between any two characteristics of a given wave (v_{wave}, *Score*, L_{wave}, and dt_{wave}) are shown in Fig. 7. These correlations indicate that, for a given wave, *Score*, v_{wave}, and L_{wave} are all closely linked. The link between *Score* and L_{wave} is intuitive, as

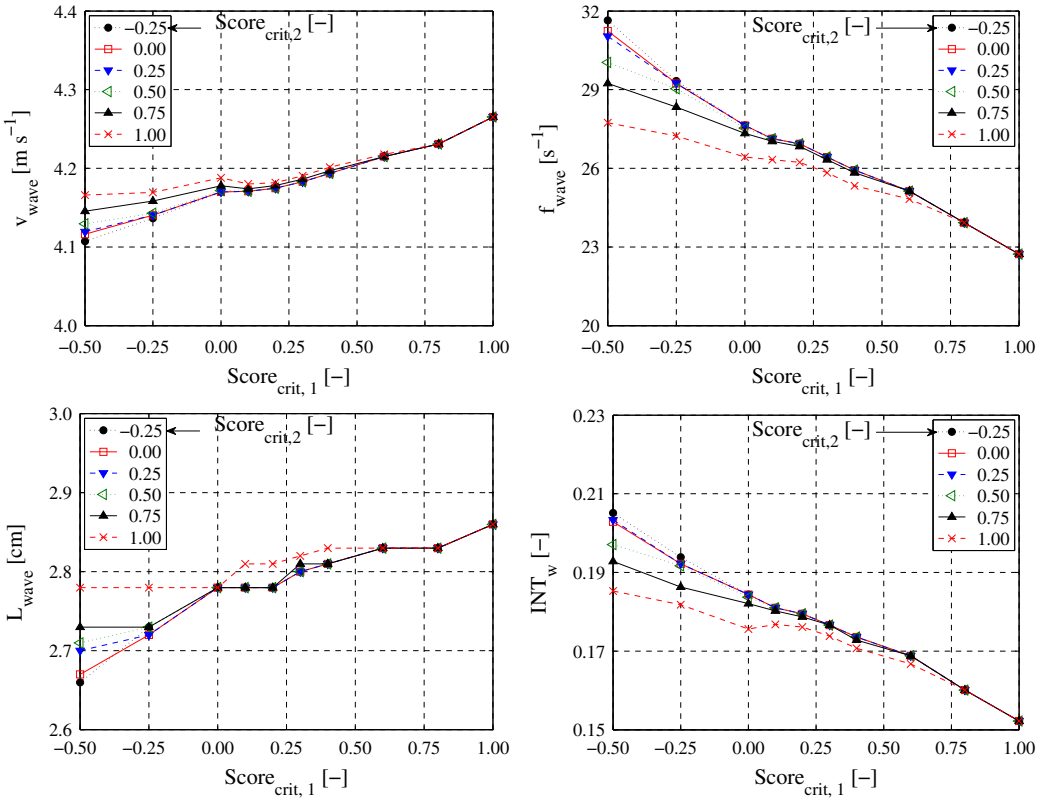

Fig. 5. Sensitivity to critical wave scores for flow with U_{sg} of 42 m s^{-1} and U_{sl} of 15.5 cm s^{-1}. (Top left) v_{wave}. (Top right) f_{wave}. (Bottom left) L_{wave}. (Bottom right) INT_w.

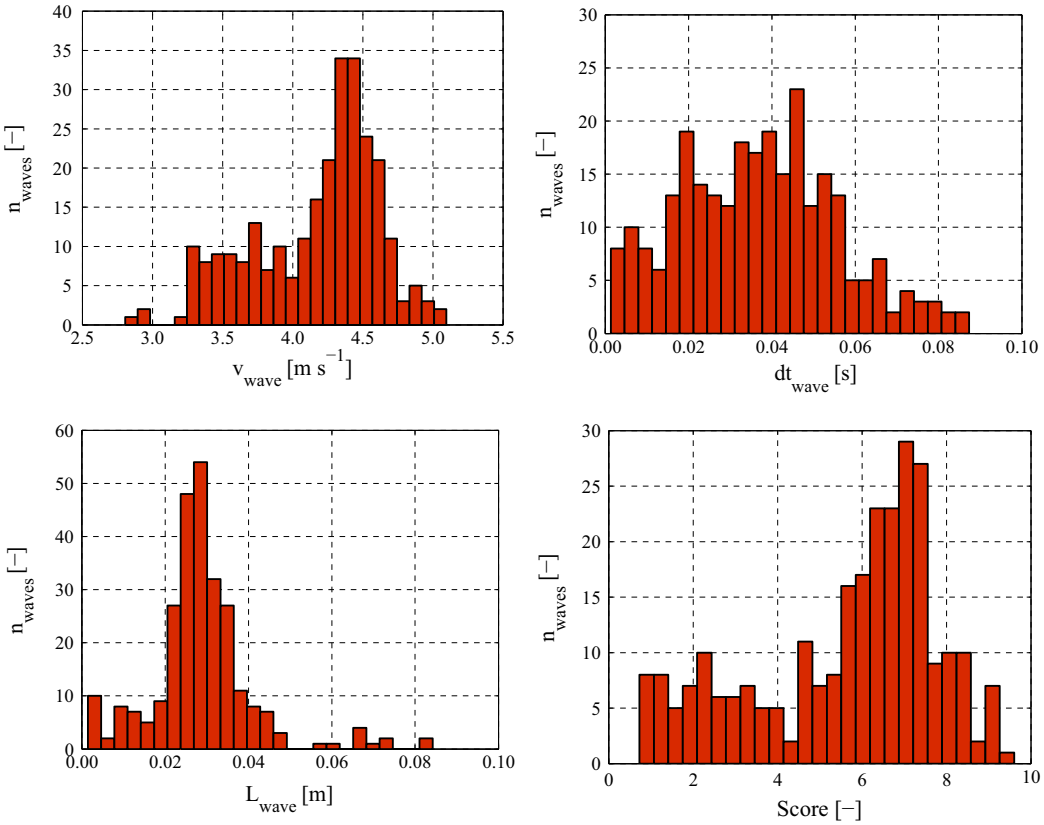

Fig. 6. Distributions (histograms) of waves in example flow. (Top left) v_{wave}. (Top right) dt_{wave}. (Bottom left) L_{wave}. (Bottom right) *Score*.

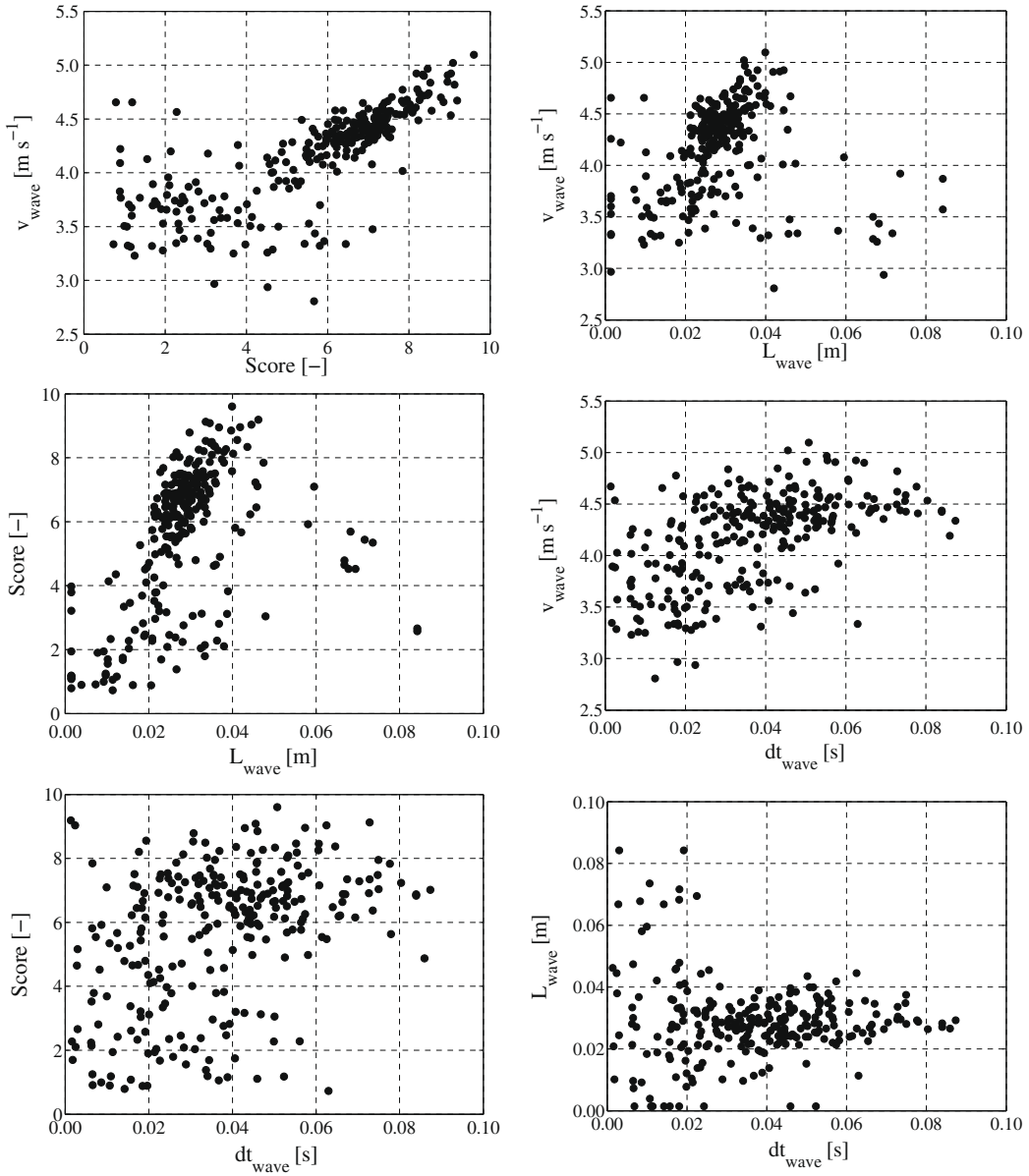

Fig. 7. Example flow, intra-wave correlations. (Top left) v_{wave} vs. *Score*. (Top right) v_{wave} vs. L_{wave}. (Middle left) *Score* vs. L_{wave}. (Middle right) v_{wave} vs dt_{wave}. (Bottom left) *Score* vs dt_{wave}. (Bottom right) L_{wave} vs. dt_{wave}.

longer waves occlude a detector for a greater period and will tend to produce higher scores. The correlation coefficient (ρ_{corr}) between these is 0.410, indicating a strong correlation. The correlation between v_{wave} and *Score* is particularly strong (ρ_{corr} of 0.750). A weaker correlation (ρ_{corr} of 0.105) exists between L_{wave} and v_{wave}.

Two types of waves are indicated. The first are longer, have a larger wave score, and travel at a higher average velocity than smaller waves. Further, these larger waves appear to form a continuum of wave sizes, with close links among L_{wave}, v_{wave}, and *Score*.

A possible physical explanation is that wave velocity is the balance point between interfacial shear (accelerates the wave) and momentum dissipation into the base film. Waves for which *Score* is higher may be those that are thicker or rougher, allowing additional momentum transfer from the gas core to the wave.

The second type of wave is smaller. For these waves, both v_{wave} and *Score* are widely distributed, with no strong link between the two; both parameters are reduced relative to larger waves. Examination of actual images indicates that these are often "piece" waves that do not appear to encircle the entire tube.

The plot comparing v_{wave} and dt_{wave} shows the two to be linked (ρ_{corr} of 0.542), with faster waves generally preceding a longer time without waves. *Score* and dt_{wave} are also linked (ρ_{corr} of 0.400). These correlations may indicate that these large, faster waves have coalesced with smaller waves that might have been immediately behind them. The effect seems to be linked most closely to the distinction between large, coherent waves and piece waves.

Fig. 8 shows the correlations between properties (v_{wave}, *Score*, L_{wave}, and dt_{wave}) of adjacent waves. In these plots, the subscripts j and $j+1$ refer to a given wave and the one after it, respectively. The plot of dt_{wave} (bottom right) is equivalent to a comparison of the wave-free periods before and after a given wave.

Any correlations between adjacent waves are weak. Those for v_{wave}, dt_{wave}, and *Score* are not statistically significant. While a statistically significant L_{wave} correlation is found in this flow condition, such a relation is not common among similar flows examined. The

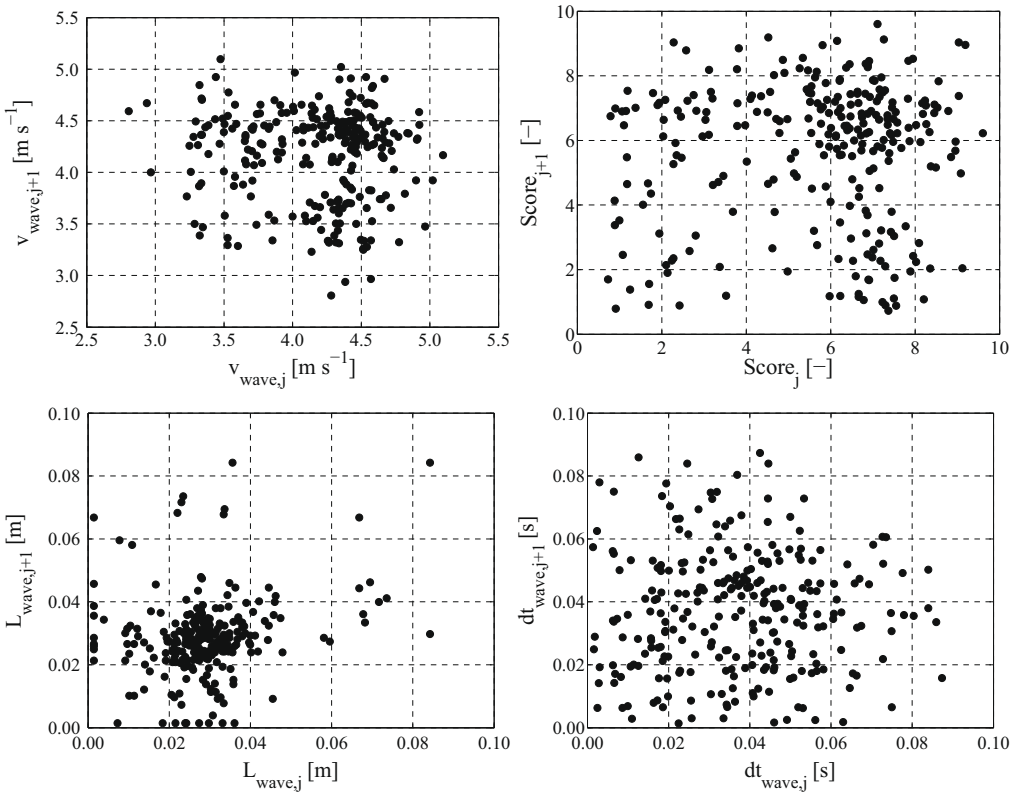

Fig. 8. Example flow, inter-wave correlations. (Top left) v_{wave}. (Top right) *Score*. (Bottom left) L_{wave}. (Bottom right) dt_{wave}.

supposed correlation is most likely an artifact of spurious L_{wave} results, as most of the results appear to be randomly distributed with respect to their neighbors. This is advantageous to modeling efforts, as waves in this flow condition might be conceptualized as independent structures.

4.2. Flow rate trends in vertical wave behavior

Flow conditions spanning a factor of more than 2 in U_{sg} and a factor of 10 in U_{sl} were studied. Figures analogous to the raw images in Fig. 3, the histograms in Fig. 6, the intra-wave correlations in Fig. 7, and the inter-wave correlations in Fig. 8 are also available for all 54 flow conditions in the electronic annex.

The most dramatic trend in wave behavior is the transition from large, coherent waves to piece waves as gas flow increases. This trend is particularly apparent in the individual waves' results for v_{wave} and *Score* and the v_{wave} vs. *Score* correlations. As discussed in Section 4.1, plots of v_{wave} vs. *Score* show two distinct regions. Among large waves, v_{wave} and *Score* are closely linked. Lower *Score* waves are piece waves, among which little relationship between *Score* and v_{wave} is seen.

Fig. 9 shows these scatterplots for 6 gas flows at a constant U_{sl} of 15.5 cm s^{-1}. At low U_{sg}, coherent waves are the dominant structure. As gas flow increases, piece waves become more dominant, with only a few large waves present at a U_{sg} of 71 m s^{-1}. As the fraction of coherent waves decreases, ρ_{corr} between v_{wave} and *Score* also decreases.

Gross wave statistics are closely linked to both gas and liquid flow rates, as shown in Fig. 10. The series in this figure are labeled by the average U_{sg} within that series; they strictly correspond to gas meter readings. The values of U_{sg} range over approximately 10% for the lowest 3 series and 25% for the highest 2 series.

v_{wave} is shown in the top two graphs, with the raw data at left and data normalized by U_{sg} at right. In general, v_{wave} increases with both gas and liquid flow rate. The range with liquid flow is somewhat small, with v_{wave} increasing by 2–3 m s^{-1} as U_{sl} increases across an order of magnitude. The dependence on U_{sg} is less than linear.

The middle graphs in Fig. 10 are also reminiscent of the trends noted for horizontal flow, in which wave frequency increases with both gas and liquid flow, at least for moderate U_{sg}. Shearer (1964) suggested that Sr_{wave} (definition repeated below) is a function of liquid flow alone.

$$Sr_{wave} = \frac{f_{wave} D}{U_{sg}} \tag{13}$$

This appears reasonable for vertical flows with U_{sg} below 60 m s^{-1}. Considering the definition of Sr_{wave}, wave frequency is approximately linear with gas flow at these flow rates. With respect to liquid flow, the wave frequency at these moderate gas flows increases by 50–100% with a factor of 10 increase in U_{sl}; at higher U_{sg}, the range in f_{wave} with liquid flow is quite narrow.

For the higher U_{sg} series, the trend in v_{wave} is not monotonic with U_{sl}. Wave velocity increases with liquid flow at low U_{sl}, then drops at intermediate U_{sl} before finally increasing above 30 cm s^{-1}. An opposite trend is apparent in f_{wave}. When taken together with manual tracking, these trends indicate that slower piece waves increase in frequency up to a U_{sl} of approximately 20 cm s^{-1} (this cut-off increases with increasing gas flow). As the liquid flow rate increases further, these piece waves do not become more frequent; instead, coherent waves become more numerous.

INT_w is dominated by the liquid flow rate. Some trends with U_{sg} are seen, but these appear to be more closely linked to the transition from piece waves to coherent waves at the higher gas flows.

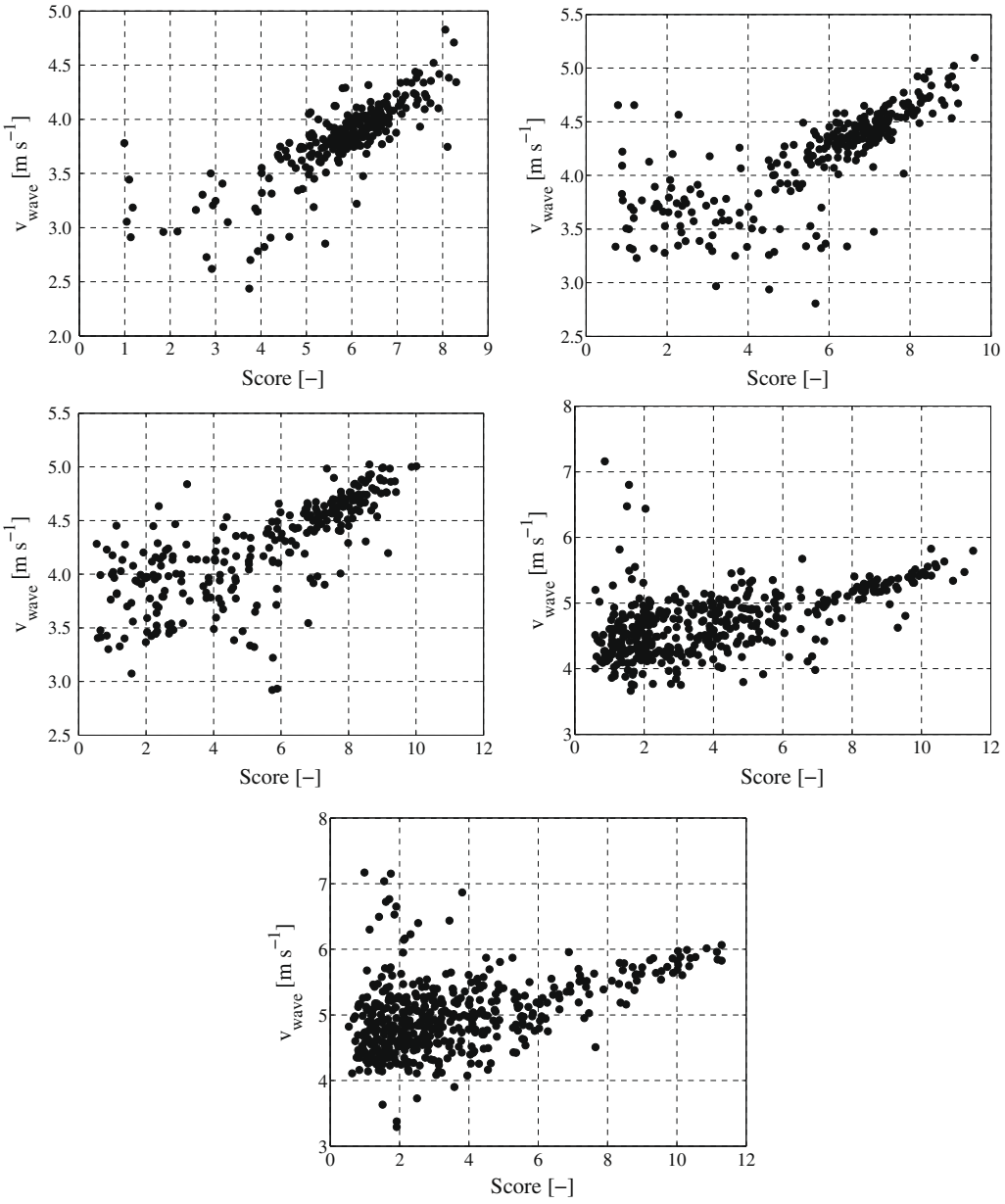

Fig. 9. v_{wave} vs. *Score*, U_{sl} =15.5 cm s^{-1}. U_{sg}:. (Top left) 33 m s^{-1}, (Top right) 42 m s^{-1}, (Middle left) 52 m s^{-1}, (Middle right) 61 m s^{-1}, (Bottom) 71 m s^{-1}.

The median L_{wave} (selected as the estimate of the average, see Section 3.8) increases in U_{sl} and decreases with U_{sg}. Once again, the transition from piece waves to coherent waves with liquid flow for high gas flow series is observed.

The values of the correlation coefficients between *Score*, v_{wave}, and L_{wave} in a given flow are primarily dependent on the preponderance of large waves over piece waves. Throughout the flow condition range studied, there is no strong link between properties of adjacent waves. They can therefore be modeled as independent structures.

5. Correlation of vertical wave statistics

Although a mechanistic model is preferable to an empirical correlation, there are a number of applications for which an empirical estimate of a wave property (*e.g.*, v_{wave}) is sufficient.

New empirical correlations for v_{wave} and f_{wave} have been developed specifically for these vertical data and are shown below. Note that the factor in parentheses of $f_{SS,vert}$ is non-dimensional.

$$v_{SS,vert} = 2.55 U_{sg} (Re_g x)^{-1/3} \tag{14}$$

$$f_{SS,vert} = 0.0056 \frac{U_{sg}}{D} \left(\frac{\rho_g U_{sg}^2}{\rho_l g D x} \right)^{1/4} \tag{15}$$

Relations for wave length and intermittency have also been developed:

$$L_{wave,SS} = 0.53 \frac{D}{x^{0.6}} \tag{16}$$

$$INT_{w,SS} = 0.1 + \frac{Re_l}{40,000} \tag{17}$$

$$Re_l = \frac{G_l D}{\mu_l} \tag{18}$$

These correlations' performance is shown in Fig. 11.

It is often useful to characterize the accuracy of a correlation using its MAE (mean absolute error), defined in the following equation. *XX* is the quantity of interest (*e.g.*, v_{wave}), n_{FC} is the number of

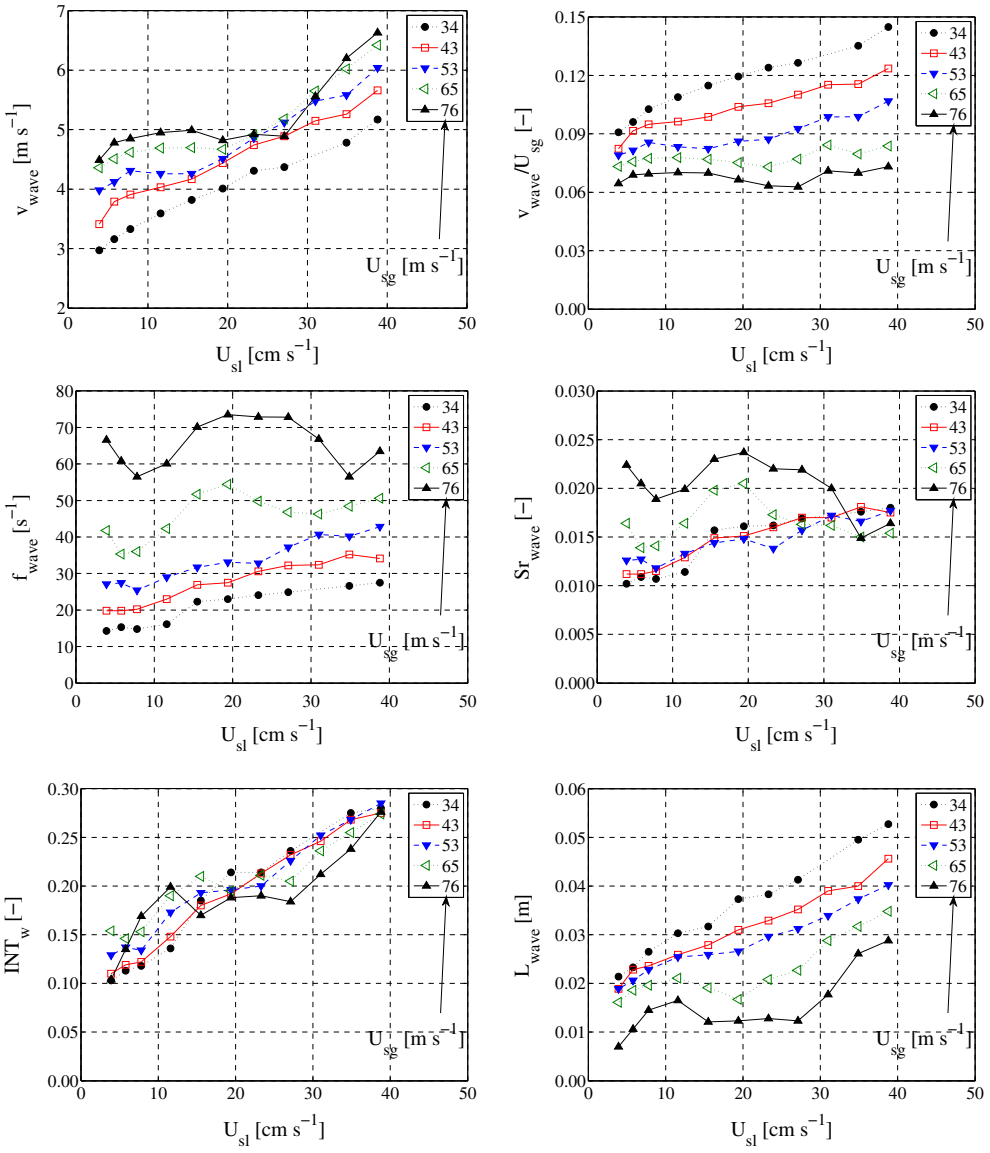

Fig. 10. Series of constant $Q_{g,nom}$, label by average U_{sg}, plotted vs. U_{sl}. (Top left) v_{wave}. (Top right) v_{wave}/U_{sg}. (Middle left) f_{wave}. (Middle right) Sr_{wave}. (Bottom left) INT_w. (Bottom right) L_{wave}.

flow conditions, and the subscripts *exp* and *corr* refer to experimental and correlated values, respectively:

$$MAE = \frac{1}{n_{FC}} \sum_{FC} \left| \frac{XX_{corr} - XX_{exp}}{XX_{exp}} \right| \times 100\% \tag{19}$$

The MAE of $v_{SS,vert}$, $f_{SS,vert}$, $L_{wave,SS}$, and $INT_{w,SS}$ with respect to these data are 5.9%, 11.6%, 19.4%, and 7.7%, respectively.

These correlations, particularly $f_{SS,vert}$ and $L_{wave,SS}$, were developed primarily for flows with U_{sg} below 70 m s^{-1} due to the non-monotonic behaviors with U_{sl} for high gas flow conditions. If the range of data is limited accordingly, the MAE results for $f_{SS,vert}$ and $L_{wave,SS}$ are reduced to 8.5% and 8.0% respectively; improvement in the correlations for INT_w and v_{wave} is also seen (7.0% and 4.8% MAE, respectively).

While these correlations were written in dimensionally-consistent forms, there are no direct data available with other flow orientations, tube diameters, pressures, temperatures, or fluid pairs to explicitly indicate the range of applicability. It is advised that these correlation be used only for low-pressure, air–water upflow data in tubes of similar diameter to the present study.

While disturbance waves have been studied by many researchers, there is a limited amount of data available in the open literature – many results are provided only in the form of graphs. Measurements of individual wave properties are nearly non-existent. The work of Hall Taylor et al. (1963) provides histograms of wave velocity and temporal spacing for an example flow; however, both U_{sg} and U_{sl} are below those in the present study by a factor of two. They also provide time-vs.-distance plots based on their video analysis that bear great similarity to that presented in Fig. 3.

Further, most disturbance wave data in the literature was taken for tubes with diameters in the range of 10 mm, a factor of two less than that in this study. One example of such data is the more recent work of Sawant et al. (2008). A subset of their data was taken at 120 kPa, similar to the pressures in the present study. While the smaller diameter provides significantly higher frequencies (factor of two) and velocities (approximately 30%), the trends with flow rates are similar at U_{sg} below 60 m s^{-1}. Above this, their data are too sparse to make meaningful comparisons.

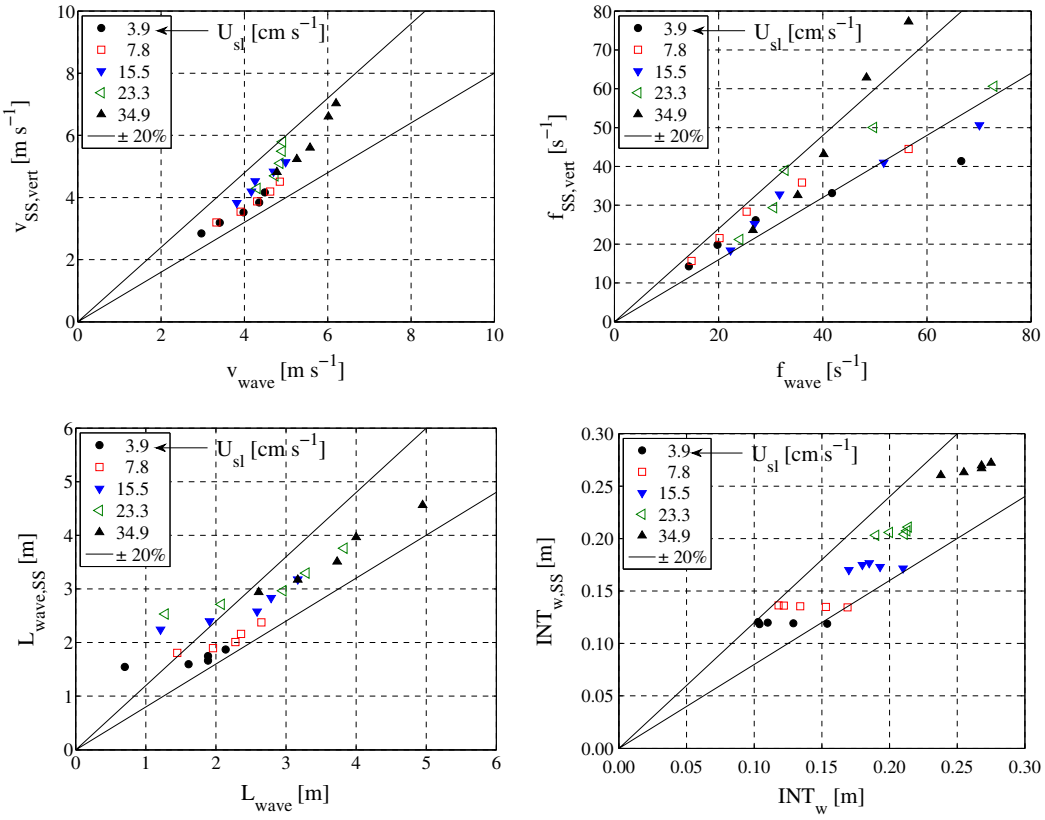

Fig. 11. Wave correlation performance, series of constant U_{sl}. (Top left) $v_{SS,vert}$. (Top right) $f_{SS,vert}$. (Bottom left) $L_{wave,SS}$. (Bottom right) $INT_{w,SS}$.

The most similar flow condition range to the present study is provided by Nedderman and Shearer (1963). Waves were studied in a 31.7 mm vertical test section with U_{sg} from 40 to 73 m s^{-1} and U_{sl} from 0.05 m s^{-1} to 0.24 m s^{-1}. By comparing Nedderman and Shearer's flows to the most similar flow condition from the present study, agreement to within 5% (MAE) is found on v_{wave}. Agreement on Sr_{wave} of 26% is found, with Nedderman and Shearer's data showing a weaker effect of gas flow rate. If only those flows with U_{sg} below 60 m^{-1} are compared, agreement to within 20% is achieved. Above this, piece waves are dominant; it is possible that Nedderman and Shearer's study did not adequately identify these smaller structures.

6. Conclusions

At least two types of wave structures exist in the range of vertical annular flows studied: large, coherent waves and smaller, less coherent waves (piece waves). A smooth transition in with gas flow occurs, with coherent waves more numerous at lower gas flows and piece waves dominant at very high gas flows. For high gas flows, the degree of piece wave dominance varies with liquid flow.

Darker waves, which have a higher *Score* by definition of this parameter, are also longer and travel at a higher velocity than lighter waves in the same flow condition. They frequently precede a shorter wave-free period (lower dt_{wave}). The distinction between piece waves and coherent waves is a factor in these statistical correlations. *Score*, v_{wave}, and L_{wave} are positively correlated when the comparison is limited to coherent waves. Correlations between adjacent waves are weak (independent structures).

As a result of these correlations, the average v_{wave} measured via ensemble averaging of individual waves and that measured from cross-correlation will disagree. A cross-correlation estimate will weight each wave's velocity differently in the averaging, depending the strength of its signal (*Score* if cross-correlation of videos/phototransistors, a combination of wave height and L_{wave} from conductance probes). Depending on the final result being modeled, different estimates of v_{wave} (method of averaging) may be appropriate. Other averaged parameters (e.g., L_{wave}) will also depend on the method of averaging employed.

Acknowledgements

The authors wish to thank Andrea Ashwood for acquiring the high-speed videos used in this work. The financial support of Bettis Laboratory is also gratefully acknowledged.

References

Azzopardi, B.J., 1986. Disturbance wave frequencies, velocities and spacing in vertical annular two-phase flow. Nucl. Eng. Design 92, 121–133.
Azzopardi, B.J., 1997. Drops in annular two-phase flow. Int. J. Multiphase Flow 23, 1–53.
Hall Taylor, N.S., Nedderman, R.M., 1968. The coalescence of disturbance waves in a annular two-phase flow. Chem. Eng. Sci. 23, 551–564.
Hall Taylor, N.S., Hewitt, G.F., Lacey, P.M.C., 1963. The motion and frequency of large disturbance waves in annular two-phase flow of air–water mixtures. Chem. Eng. Sci. 18, 537–552.
Hawkes, N.J., Lawrence, C.J., Hewitt, G.F., 2000. Studies of wispy-annular flow using transient pressure gradient and optical measurements. Int. J. Multiphase Flow 26, 1565–1582.
Martin, C.J., 1983. Annular two phase flow. D. Phil. Thesis, University of Oxford, UK.
Mori, K., Kaji, M., Kondo, Y., Sekoguchi, K., 1996. Wave venation in downward gas–liquid two-phase flow (Part I, Time-spatial behavior chart of interface and analysis of main wave-vein). Heat Transfer – Jpn. Res. 25, 499–510.
Mori, K., Kondo, Y., Kaji, M., Yagishita, T., 1999. Effects of liquid viscosity on characteristics of waves in gas–liquid two-phase flow (characteristics of huge waves and disturbance waves). JSME Int. J. Ser. B – Fluids Thermal Eng. 42, 658–666.
Nedderman, R.M., Shearer, C.J., 1963. The motion and frequency of large disturbance waves in annular two-phase flow of air–water mixtures. Chem. Eng. Sci. 18, 661–670.

Pearce, D.L., 1979. Film waves in horizontal annular flow: space–time correlator experiments. CERL Note RD/L/N111/79.
Sawai, T., Yamauchi, S., Nakanishi, S., 1989. Behavior of disturbance waves under hydrodynamic non-equilibrium conditions. Int. J. Multiphase Flow 15, 341–356.
Sawant, P., Ishii, M., Hazuki, T., Takamasa, T., Mori, M., 2008. Properties of disturbance waves in vertical annular two-phase flow. Nucl. Eng. Design 238, 3528–3541.
Schubring, D., Shedd, T.A., 2008. Wave behavior in horizontal annular air–water flow. Int. J. Multiphase Flow 34, 636–646.
Shearer, C.J., 1964. PhD thesis, University of Cambridge, Cambridge, UK.
Swanson, R.W., 1966. Characteristics of the gas–liquid interface in two-phase annular flow. PhD thesis, University of Delaware, Newark, DE, USA.
Wolf, A., Jayanti, S., Hewitt, G.F., 2001. Flow development in vertical annular flow. Chem. Eng. Sci. 56, 3221–3235.